Avoided level crossing at the magnetic field induced topological phase transition due to spin-orbital mixing

G. Krizman,[1] B. A. Assaf,[2,3] M. Orlita,[4,5] T. Phuphachong,[1] G. Bauer,[6] G. Springholz,[6] G. Bastard,[1] R. Ferreira,[1] L. A. de Vaulchier,[1] and Y. Guldner[1]

[1]*Laboratoire Pierre Aigrain, Département de Physique, Ecole Normale Supérieure, PSL Research University, Sorbonne Université, CNRS, 24 rue Lhomond, 75005 Paris, France*

[2]*Département de Physique, Ecole Normale Supérieure, PSL Research University, CNRS, 24 rue Lhomond, 75005 Paris, France*

[3]*Department of Physics, University of Notre Dame, Notre Dame, Indiana 46556, USA*

[4]*Laboratoire National des Champs Magnétiques Intenses, CNRS-UJF-UPS-INSA, 38042 Grenoble, France*

[5]*Institute of Physics, Charles University, Ke Karlovu 5, 12116 Praha 2, Czech Republic*

[6]*Institüt für Halbleiter- und Festkörperphysik, Johannes Kepler Universität, Altenbergerst. 69, 4040 Linz, Austria*

In three-dimensional topological insulators, an effective closure of the bulk energy gap with increasing magnetic field expected at a critical point can yield a band crossing at a gapless Dirac node. Using high-field magneto-optical Landau-level spectroscopy on the topological crystalline insulator $Pb_{1-x}Sn_xSe$, we demonstrate that such a gap closure does not occur, and an avoided crossing is observed as the magnetic field is swept through the critical field. We attribute this anticrossing to orbital parity and spin mixing of the $N = 0$ levels. Concurrently, we observe no gap closure at the topological phase transition versus temperature suggesting that both are due to a single, likely extrinsic, mechanism.

The search for Dirac fermions beyond two dimensions (2D) [1–4] has stimulated investigations of tunable topological material [5–12] that possess an energy gap that can be varied from negative through zero to positive using external knobs as illustrated in Fig. 1(a). The zero-gap state at the phase boundary between the trivial and topological phase is expected to be a realization of a critical three-dimensional (3D) Dirac state. The thermodynamic stability of this critical point is essential to our fundamental understanding of topological phase transitions [13–17] and our realization of Dirac fermions beyond 2D. One particularly striking feature of topological materials is the inverted behavior of their $N = 0$ Landau levels (LLs) versus magnetic field [4,9,13,18–20]. In such systems, the $N = 0$ conduction LL decreases in energy when the magnetic field increases, whereas the $N = 0$ valence level increases [see Fig. 1(b)]. This leads to an effective closure of the energy gap and a topological phase transition at a critical field B_c. Although previously studied in 2D for HgTe quantum wells [13,21–23], this transition has not been observed in 3D topological systems as most of those have large energy gaps requiring B_c in excess of 100 T [24]. This problem can be alleviated using IV-VI topological crystalline insulators (TCIs), in which the energy gap can be tuned close to zero by choice of the proper composition [7–9,11,14].

In this work, we therefore study the critical behavior of the 3D TCI $Pb_{1-x}Sn_xSe$ as a function of magnetic field in the vicinity of the critical point B_c of the topological transition, which occurs at $B = 25$ T for x = 0.19 [11]. The mirrorlike band structure [11,19] of $Pb_{1-x}Sn_xSe$ yields linear $N = 0$ LLs in the entire magnetic field range of interest, and can thus result in a clear-cut determination of B_c and the behavior around it. Using a detailed analysis of

magneto-optical transitions and their oscillator strengths, we thus demonstrate the presence of an avoided crossing of the $N = 0$ conduction and valence Landau levels at the critical field B_c as illustrated in Fig. 1(c). This anticrossing unambiguously manifests itself via the appearance of otherwise forbidden magneto-optical transitions that clearly violate conventional selection rules. We attribute this violation to the presence of spin-orbit mixing of the $N = 0$ LL near B_c. We also show that the anticrossing is present at all temperatures in the topological regime as well as for the topological phase transition as a function of temperature. Considering the crystalline and dielectric properties of $Pb_{1-x}Sn_xSe$, we can rule out (i) bulk inversion asymmetry, (ii) electron-phonon interaction, (iii) electron-electron interactions, and (iv) surface effects [14] as a possible origin for the anticrossing. We thus discuss our findings in light of recent proposals on the role of alloy disorder [17] and fundamental thermodynamic effects that yield a topological phase transition without a gap closure [25].

Magneto-optical Landau-level spectroscopy measurements are performed on high-quality [111]-oriented $Pb_{1-x}Sn_xSe$ epilayers grown by molecular beam epitaxy as described in our previous work [11,26]. Two 2-μm-thick samples with composition x = 0.19 and x = 0.14, respectively, above and below the topological phase transition at 4.2 K, are studied. Magnetospectroscopy is performed in transmission mode in the Faraday geometry versus magnetic field and temperature. We use a setup analogous to one used in our previous works [11,27] with a composite Si bolometer mounted behind the sample for measurements below 4.2 K at the Laboratoire National des Champs Magnétiques Intenses in Grenoble up to 34 T. The probe is equipped with ZnSe windows with
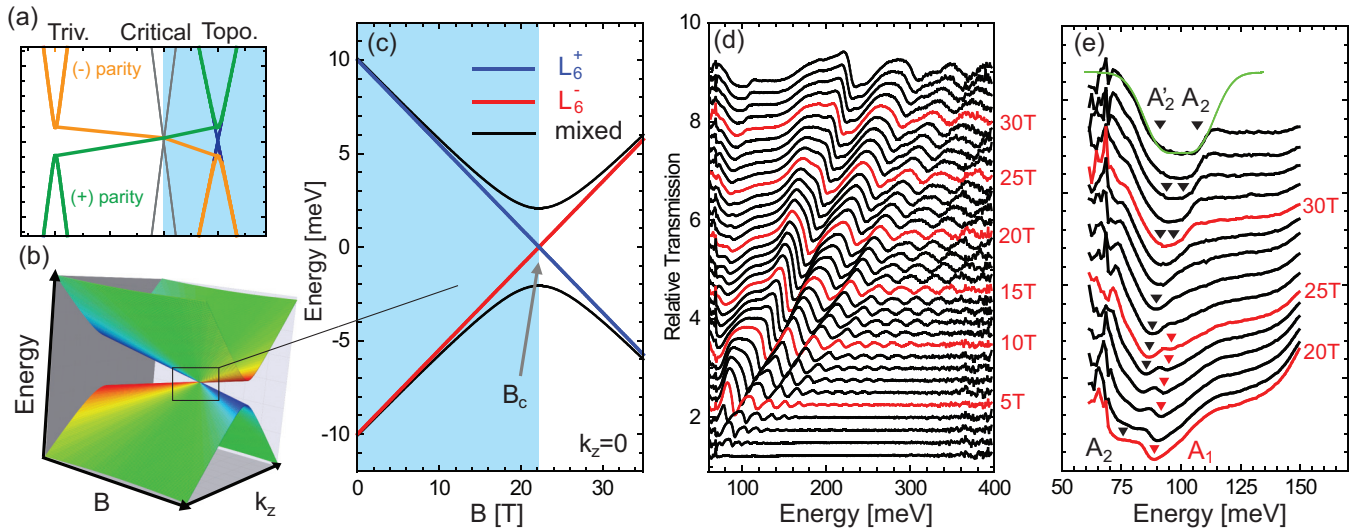
FIG. 1. (a) Topological phase transition from trivial to topological with the critical gapless state shown in gray. The blue shade indicates the topological regime. (b) Evolution of the bulk $N = 0$ Landau levels as a function of magnetic field for a topological system. The color indicates the $L_6^{\pm,\downarrow,\uparrow}$ orbital character of the $N = 0$ levels. (c) Zoom-in on the region at $k_z = 0$ showing crossing LL with pure $L_6^{\pm}$ character in blue and red and the anticrossing LL with mixed $L_6^{\pm}$ character in black. (d) Magneto-optical transmission $[T(B)/T(0)]$ spectra measured in Pb$_{1-x}$Sn$_x$Se ($x = 0.19$) versus magnetic field between 2 and 34 T at 1.6 K. Red curves mark magnetic fields that are multiple of 5 T and the curves are arbitrarily shifted vertically for clarity. (e) Zoom-in on the low-energy region between 20 and 34 T highlighting the behavior of three particular transitions labeled A_1, A_2, and A_2'. A multipeak fit shown in green is used to separate A_2' and A_2 at high fields.

an energy cutoff close to 60 meV. Temperature dependent measurements up to 200 K are performed at Ecole Normale Supérieure up to 17 T using a second setup with external detectors (far-IR bolometer or HgCdTe mid-IR detector).

Figure 1(d) shows magneto-optical spectra obtained for Pb$_{0.81}$Sn$_{0.19}$Se, between $B = 2$ T and $B = 34$ T at 1.6 K, up to 400 meV. Pronounced transmission minima originating from LL transitions are observed. A zoom-in on the low-energy section of the spectra for fields between 20 and 34 T is shown in Fig. 1(e). A strong transmission minimum (A_1) marked by the red arrow is observed below 100 meV and decreases in amplitude as B approaches 25T. A second minimum (A_2) occurring at lower energy marked by a black arrow gains in amplitude and becomes dominant at very high fields. This transition widens above ~28 T, as it splits into two transitions. A multipeak fit allows one to separate the two transitions, and pinpoint the position of A_2 and A_2' as shown in Fig. 1(e). The behavior observed in Fig. 1(e) is unique to the topological sample and is *not* observed for the topologically trivial Pb$_{0.86}$Sn$_{0.14}$Se sample as shown in the Supplemental Material [28].

Next, we will show that the three transmission minima and their changing amplitudes and energies versus magnetic field are direct evidence of the topological phase transition that occurs after an avoided crossing of the valence and conduction $N = 0$ LLs at B_c [Fig. 1(c)]. To this end, we compute the LL spectrum using the $\mathbf{k} \cdot \mathbf{p}$ method introduced by Mitchell and Wallis [29] detailed in our previous work [11]. In Pb$_{1-x}$Sn$_x$Se the band extrema occur at the L points of the Brillouin zone and the orbital basis near the band edges consists of two bands of opposite parity referred to as $L_6^{\pm}$ [29–31]. The interaction between these two bands perturbed by higher order bands

that are farther away from the band edge [29,31,32] yields a massive Dirac-like band structure [9,11,33]. In the topological state, the conduction band is L_6^+ and the valence band is L_6^- [7,34]. In this case, the LL energy is given by

$$E_{N>0}^{c,\uparrow/\downarrow} = \pm\hbar\tilde{\omega} + \sqrt{(\Delta - \hbar\tilde{\omega}N)^2 + 2v_c^2\hbar eBN},$$

$$E_{N=0}^{c,\downarrow} = \Delta - \hbar\tilde{\omega},$$

$$E_N^{v,\uparrow/\downarrow} = \pm\hbar\tilde{\omega} - \sqrt{(\Delta - \hbar\tilde{\omega}N)^2 + 2v_c^2\hbar eBN},$$

$$E_{N=0}^{v,\uparrow} = -\Delta + \hbar\tilde{\omega}. \tag{1}$$

Here $\Delta(>0)$ is the half-energy gap, v_c is the Dirac velocity related to the $\mathbf{k} \cdot \mathbf{p}$ matrix element, and $\hbar\tilde{\omega} = \hbar eB/\tilde{m}$ where $\tilde{m}$ includes the far-band contribution to the band-edge mass and the g factor $\tilde{g} = |2m_0/\tilde{m}|$ [9]. N is the Landau index, c/v is the conduction/valence band index and the $\downarrow/\uparrow$ index denotes the "effective spin" introduced by Mitchell and Wallis [28–30,35]. The LLs are plotted versus magnetic field in Fig. 2(a) up to 34 T. The $N = 0$ levels are linear in B and (anti-) cross at B_c, i.e., when $\hbar\tilde{\omega} = \Delta$. Beyond B_c the two levels interchange.

Note that only transitions pertaining to the levels of the oblique valleys of (111)-oriented Pb$_{1-x}$Sn$_x$Se are considered as they are dominant in the optical absorption for $x = 0.19$. The valley anisotropy is very small [31] rendering the valley splitting only visible at very high fields. Interband magneto-optical transitions between the LLs given in Fig. 2(a) verify the selection rules $\Delta N = \pm 1$ and conservation of effective spin [11,28,29,31], so that the transition energies are those of
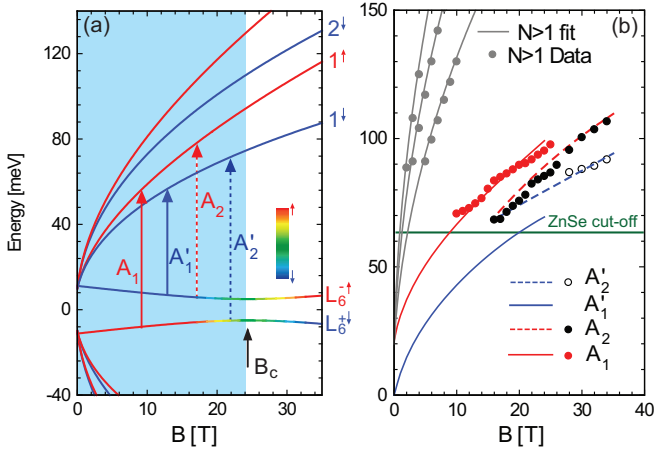
FIG. 2. (a) LL energy versus magnetic field computed using Eq. (1). The effective spin-"up" (-"down") levels are plotted in red (blue). The hybridized $N = 0$ levels are plotted with a color gradient that illustrates their spin-orbital mixing. B_c is the critical field. The A_1, A_2, A_1', and A_2', transitions are shown as full or broken arrows in red and blue. The blue shade indicates the topological regime. (b) Magneto-optical transition fan chart at low energies up to $B = 34$ T. Red dots correspond to the A_1 absorption data points, the full black ones to A_2, and the empty circles to A_2'. The solid red and blue curves correspond to the calculated variation of A_1 and A_1' and the dashed red and blue curves to that of A_2 and A_2', respectively. The gray dots and lines are data points and curve fits using Eq. (2) for transitions not involving the $N = 0$ levels ($N > 1$). The green line represents the cutoff of the ZnSe Grenoble probe window.

a massive Dirac spectrum:

$$
\begin{aligned}
& E_N^{c,\uparrow/\downarrow} - E_{N \pm 1}^{v,\uparrow/\downarrow} \\
& = \sqrt{(\Delta - \hbar\tilde{\omega}N)^2 + 2v_c^2 \hbar e B N} \\
& \quad + \sqrt{[\Delta - \hbar\tilde{\omega}(N \pm 1)]^2 + 2v_c^2 \hbar e B(N \pm 1)}.
\end{aligned} \tag{2}
$$

For $N = 1$, we get a transition energy from $N = 0^v$ to $N = 1^{c,\uparrow}$ referred to as the A_1 transition [see Fig. 2(a)]. For $B < B_c$, i.e., $\hbar\tilde{\omega} < \Delta$, this is the dominant interband transition. As $N = 0^v$ is ideally pure of effective spin and orbital character ($L_6^{-,\uparrow}$) [29], the transition to $N = 1^{c,\uparrow}$ is the only one allowed if the conventional [11,31,32] selection rules are obeyed. Similarly, the only intraband transition that is allowed is the $N = 0^c$ to $N = 1^{c,\downarrow}$ referred to as the A_1' transition [see Fig. 2(a)]. Two additional transitions, the $N = 0^{v,\uparrow}$ to $N = 1^{c,\downarrow}$ and the $N = 0^{c,\downarrow}$ to $N = 1^{c,\uparrow}$ shown as dashed arrows (A_2 and A_2') are not allowed as they do not conserve the effective spin, if the $N = 0$ levels do not hybridize.

The hybridization of the $N = 0$ levels results in an anti-crossing which renormalizes their energy:

$$
E_{N=0}^{c/v} = \pm\sqrt{(\Delta - \hbar\tilde{\omega})^2 + W^2}. \tag{3}
$$

Here, W is the hybridization energy. The renormalized $N = 0$ levels computed using Eq. (3) are shown in Fig. 2(a) with the respective orbital weight illustrated by a color gradient.

Accordingly, the A_1 transition is shifted in energy:

$$
E_{A1} = \sqrt{(\Delta - \hbar\tilde{\omega})^2 + 2v_c^2 \hbar e B} + \sqrt{(\Delta - \hbar\tilde{\omega})^2 + W^2}. \tag{4}
$$

This hybridization also leads to spin and orbital mixing of the two levels and to the activation of the A_2 and A_2' transitions near B_c as shown in Fig. 2(a).

From the data in Figs. 1(d) and 1(e), we construct a fan diagram and fit the magneto-optical transitions with the calculated LLs. One free fit parameter (W) is needed for transitions involving the $N = 0$ levels. Using transitions involving higher N, the energy gap and velocity are found to be $2\Delta = 20$ meV, $v_c = 4.7 \times 10^5$ m/s [see Fig. 2(b) and Supplemental Material [28]]. $\tilde{m}$ is fixed to $0.28m_0$, in agreement with previous studies [19,31] and to yield $B_c \approx 24$ T, the field at which A_1 and A_2 are almost equal in amplitude. The transition energies for A_1, A_2, and A_2' are plotted versus magnetic field in Fig. 2(b) along with $N > 1$ transitions. Curve fits using theoretically calculated transitions that take into account the renormalized $N = 0$ levels yield an excellent agreement with experiment for $W = (5 \pm 1)$ meV as shown in Fig. 2(b).

For $B < B_c$, the A_1 transition is strongest, as seen in Fig. 1(e). We do not observe the A_1' intraband transition in this regime, since it falls in an energy region that is not within experimental reach (below 60 meV). A_2 emerges near 17 T and gains in amplitude relative to A_1. A_2' then splits from A_2 close to 28 T. This splitting corresponds to the point where the energy separation between A_2 and A_2' becomes larger than the transition linewidth. For $B > B_c$, A_2 and A_2' gain in amplitude and become dominant while A_1 is suppressed [Fig. 1(e)] since the $N = 0$ LLs alter their spin and orbital character as seen in Figs. 2(a) and 2(b).

In order to shed light on the orbital nature of the $N = 0$ levels, the ratio of the oscillator strength of the A_1 and A_2 transitions is computed using their matrix elements at each field. This ratio is mainly imposed by the evolution of the $L_6^{+,\downarrow}$ to $L_6^{-,\uparrow}$ component for the $N = 0^{c/v}$ Landau level. It is derived in the Supplemental Material [28] and given by

$$
\left(\frac{A_2}{A_1}\right) = \frac{\left(\Delta - \hbar\tilde{\omega} - \sqrt{(\Delta - \hbar\tilde{\omega})^2 + |W|^2}\right)^2}{|W|^2}. \tag{5}
$$

Equation (5) allows us to quantify the mixing of the $N = 0$ levels. Figure 3(a) shows the comparison between Eq. (5) and the experimental absorption amplitude ratio A_2/A_1 extracted by fitting the spectra shown in Fig. 1(e). The agreement is remarkable, up to 25 T, the field at which A_1 can still be reliably extracted. The consequences of this result are of major fundamental importance, as they allow a direct experimental determination of the changing spin-orbital character of each level, and therefore of the effective evolution of the topological state of the system with magnetic field. When the ratio is smaller than 1, the system is nontrivial, meaning that the conduction $N = 0$ is dominantly $L_6^{+,\downarrow}$ and the valence level $L_6^{-,\uparrow}$. When it exceeds 1, the character is reinverted and trivial parity is smoothly restored.

Note that we have only probed the transition that occurs for the oblique valleys of $Pb_{1-x}Sn_xSe$. $\tilde{m}$, and therefore B_c, are slightly valley dependent [31]. Hence, the transition for the longitudinal valley can occur at a field slightly lower than for the oblique ones. Accordingly, there has to exist an
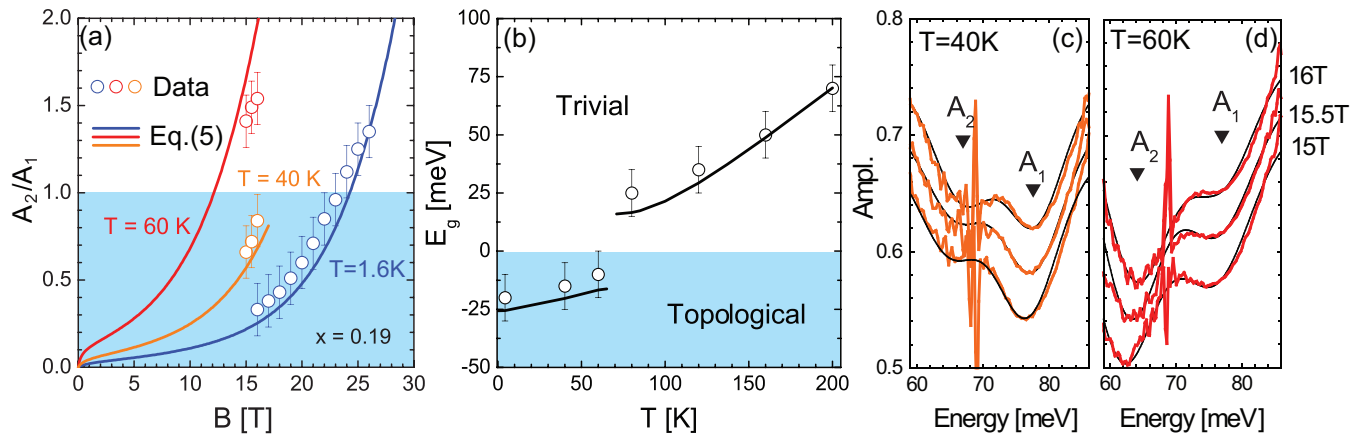
FIG. 3. (a) Relative amplitude of A_2 to A_1 (empty circles) compared with the relative oscillator strength (solid lines) calculated using Eq. (5) for $T = 1.6$, 40, and 60 K for $Pb_{0.81}Sn_{0.19}Se$. (b) Energy gap versus temperature for $Pb_{0.81}Sn_{0.19}Se$. Empty circles are data points and the solid line is calculated using Eq. (6). (c),(d) Magneto-optical spectra measured between 15 and 16 T for $T = 40$ and 60 K, respectively. The A_1 and A_2 transitions are highlighted. A Gaussian-broadened multipeak fit to the data is shown in black.

intermediate phase where the system is topologically similar to a Z_2-topological insulator with three inverted bands, before becoming trivial.

Measurements at higher temperature (up to 200 K) demonstrate the evolution of A_1 and A_2 through the topological phase transition in Fig. 3. Topological $Pb_{1-x}Sn_xSe$ exhibits a closure of the energy gap as temperature is increased, with a critical temperature of $T \approx 70$ K for $x = 0.19$ [14,34]. Magneto-optical measurements were performed to follow the variation of the energy gap, and track the changing amplitude of A_2 and A_1 near B_c up to $T = 200$ K. Corresponding fan charts are shown in the Supplemental Material [28]. The experimental variation of the gap across the topological phase transition at $T = 70$ K is plotted in Fig. 3(b).

In the topological regime, the energy gap is -15 meV at 40 K and -10 meV at 60 K [Fig. 3(b)]. Low-energy spectra taken at 40 and 60 K are shown in Figs. 3(c) and 3(d), highlighting the evolution of A_2 and A_1 versus temperature and magnetic field. Assuming $\tilde{m}$ does not change with temperature, we expect $B_c \approx 18$ T at 40 K and $B_c \approx 12$ T at 60 K. The changing amplitude of A_2 and A_1 can be observed in both cases between 15 and 16 T. At 40 K, $B = 16$ T remains smaller than B_c, therefore A_1 remains strongest and weakens as the field is increased as seen in Fig. 3(c). At 60 K, B_c drops to 12 T. By 15 T($> B_c$), the system has already undertaken a partial parity reinversion and A_2 becomes stronger than A_1 as seen in Fig. 3(d). The amplitude ratio A_2/A_1 for those two temperatures is shown in Fig. 3(a) and compared to the calculated oscillator strength. The parameters used for the calculation are identical to those used at 1.6 K, apart from E_g which is taken from Fig. 3(b). The agreement between the calculation and the data is excellent at all temperatures in Fig. 3(a), confirming the presence of spin-orbital mixing near B_c for any given temperature at which the system is nontrivial.

Note that in the trivial phase ($T \geqslant 70$ K or for $Pb_{0.86}Sn_{0.14}Se$ [28]), we do not observe the behavior attributed to the mixing since magneto-optical transitions obey conventional selection rules [11]. This further confirms our interpretation relating the emergence of forbidden transitions to spin-orbital mixing. Overall, our experimental

results allow us to quantitatively extract the degree of mixing and to demonstrate a smooth topological-to-trivial transition with an anticrossing at B_c.

In Fig. 3(b), it is also interesting to notice the absence of gap closure for the temperature induced topological phase transition, previously suggested by angle-resolved photoemission spectroscopy measurements on $Pb_{1-x}Sn_xSe$ single crystals [14]. Near the critical temperature T_c, this anticrossing W' is extracted by fitting the variation of the gap versus temperature with the following empirical equation as shown in Fig. 3(b):

$$\tilde{E}_g(T) = \pm\sqrt{E_g(T)^2 + 4W'^2}. \tag{6}$$

Here, $E_g(T) = E_g(4.2 \text{ K}) - 32 + \sqrt{32^2 + 0.58^2 T^2}$. The $\pm$ sign is for trivial and topological, respectively. We find $W' = (8 \pm 1)$meV of the same order of magnitude as W, suggesting that both are caused by a single mechanism. Note that for two-dimensional HgTe quantum wells the anticrossing of the $N = 0$ LLs has been attributed either to inversion asymmetry or to electron-electron interactions [13,15,19]. Rocksalt $Pb_{1-x}Sn_xSe$ is, however, inversion symmetric and exhibits a huge dielectric constant [36] ruling out both mechanisms [13,15,19,37]. Moreover, the nearly temperature independent W also rules out the role of electron-phonon interactions. Previous magneto-optical work on Bi proposed a field-dependent W as a coupling term stemming from time-reversal-symmetry breaking [38–40]. This, however, cannot explain our anticrossing observed versus temperature. Thus, overall, we are able to retain either an extrinsic mechanism such as alloy disorder [17] or atomic vacancies or a thermodynamic first-order transition as proposed in Ref. [25] as the possible origin for W and W'. Further systematic measurements on samples with controlled level of disorder and theoretical work are required to resolve this issue.

To conclude, magneto-optical measurements at high magnetic fields evidence a topological phase transition induced by the field with an avoided crossing at the critical point. The avoided crossing arises from spin-orbital mixing that occurs when the $N = 0$ LL converge toward each other at high

field. This effect is observed concurrently with a temperature induced topological phase transition without gap closure. The absence of gap closure versus temperature and the anticrossing near B_c are likely due to a single mechanism that mixes levels that are otherwise of opposite parity. Elucidating the origin of topological phase transitions without gap closure is of fundamental importance and will contribute to realizing critical 3D gapless Dirac modes using tunable topological materials.

[1] M. Neupane, S.-Y. Xu, R. Sankar, N. Alidoust, G. Bian, C. Liu, I. Belopolski, T.-R. Chang, H.-T. Jeng, H. Lin, A. Bansil, F. Chou, and M. Z. Hasan, Nat. Commun. **5**, 3786 (2014).

[2] J. Xiong, S. K. Kushwaha, T. Liang, J. W. Krizan, M. Hirschberger, W. Wang, R. J. Cava, and N. P. Ong, Science **350**, 413 (2015).

[3] I. Belopolski, S. Y. Xu, N. Koirala, C. Liu, G. Bian, V. N. Strocov, G. Chang, M. Neupane, N. Alidoust, D. Sanchez, H. Zheng, M. Brahlek, V. Rogalev, T. Kim, N. C. Plumb, C. Chen, F. Bertran, P. Le Fèvre, A. Taleb-Ibrahimi, M. C. Asensio, M. Shi, H. Lin, M. Hoesch, S. Oh, and M. Z. Hasan, Sci. Adv. **3**, 12 (2017).

[4] M. Konig, S. Wiedmann, C. Brune, A. Roth, H. Buhmann, L. W. Molenkamp, X.-L. Qi, and S.-C. Zhang, Science **318**, 766 (2007).

[5] S.-Y. Xu, Y. Xia, L. A. Wray, S. Jia, F. Meier, J. H. Dil, J. Osterwalder, B. Slomski, A. Bansil, H. Lin, R. J. Cava, and M. Z. Hasan, Science **332**, 560 (2011).

[6] T. Sato, K. Segawa, K. Kosaka, S. Souma, K. Nakayama, K. Eto, T. Minami, Y. Ando, and T. Takahashi, Nat. Phys. **7**, 840 (2011).

[7] P. Dziawa, B. J. Kowalski, K. Dybko, R. Buczko, A. Szczerbakow, M. Szot, E. Łusakowska, T. Balasubramanian, B. M. Wojek, M. H. Berntsen, O. Tjernberg, and T. Story, Nat. Mater. **11**, 1023 (2012).

[8] P. S. Mandal, G. Springholz, V. V. Volobuev, O. Caha, A. Varykhalov, E. Golias, G. Bauer, O. Rader, and J. Sánchez-Barriga, Nat. Commun. **8**, 968 (2017).

[9] B. A. Assaf, T. Phuphachong, E. Kampert, V. V. Volobuev, P. S. Mandal, J. Sánchez-Barriga, O. Rader, G. Bauer, G. Springholz, L. A. de Vaulchier, and Y. Guldner, Phys. Rev. Lett. **119**, 106602 (2017).

[10] L. Wu, M. Brahlek, R. Valdés Aguilar, A. V. Stier, C. M. Morris, Y. Lubashevsky, L. S. Bilbro, N. Bansal, S. Oh, and N. P. Armitage, Nat. Phys. **9**, 410 (2013).

[11] B. A. Assaf, T. Phuphachong, V. V. Volobuev, G. Bauer, G. Springholz, L.-A. de Vaulchier, and Y. Guldner, npj Quant. Mater. **2**, 26 (2017).

[12] T. H. Hsieh, H. Lin, J. Liu, W. Duan, A. Bansil, and L. Fu, Nat. Commun. **3**, 982 (2012).

[13] M. Orlita, K. Masztalerz, C. Faugeras, M. Potemski, E. G. Novik, C. Brüne, H. Buhmann, and L. W. Molenkamp, Phys. Rev. B **83**, 115307 (2011).

[14] B. M. Wojek, P. Dziawa, B. J. Kowalski, A. Szczerbakow, A. M. Black-Schaffer, M. H. Berntsen, T. Balasubramanian, T. Story, and O. Tjernberg, Phys. Rev. B **90**, 161202 (2014).

[15] A. V. Ikonnikov, S. S. Krishtopenko, O. Drachenko, M. Goiran, M. S. Zholudev, V. V. Platonov, Y. B. Kudasov, A. S.

Korshunov, D. A. Maslov, I. V. Makarov, O. M. Surdin, A. V. Philippov, M. Marcinkiewicz, S. Ruffenach, F. Teppe, W. Knap, N. N. Mikhailov, S. A. Dvoretsky, and V. I. Gavrilenko, Phys. Rev. B **94**, 155421 (2016).

[16] M. Salehi, H. Shapourian, N. Koirala, M. J. Brahlek, J. Moon, and S. Oh, Nano Lett. **16**, 5528 (2016).

[17] W. Zhang, M. Chen, J. Dai, X. Wang, Z. Zhong, S.-W. Cheong, and W. Wu, Nano Lett. **18**, 2677 (2018).

[18] B. A. Bernevig and T. L. Hughes, *Topological Insulator and Topological Superconductors* (Princeton University Press, Princeton, NJ, 2013).

[19] A. Calawa, J. Dimmock, T. Harman, and I. Melngailis, Phys. Rev. Lett. **23**, 7 (1969).

[20] M. Schultz, U. Merkt, A. Sonntag, U. Rossler, R. Winkler, T. Colin, P. Helgesen, T. Skauli, and S. Lovold, Phys. Rev. B **57**, 14772 (1998).

[21] M. Marcinkiewicz, S. Ruffenach, S. S. Krishtopenko, A. M. Kadykov, C. Consejo, D. B. But, W. Desrat, W. Knap, J. Torres, A. V. Ikonnikov, K. E. Spirin, S. V. Morozov, V. I. Gavrilenko, N. N. Mikhailov, S. A. Dvoretskii, and F. Teppe, Phys. Rev. B **96**, 035405 (2017).

[22] A. M. Kadykov, S. S. Krishtopenko, B. Jouault, W. Desrat, W. Knap, S. Ruffenach, C. Consejo, J. Torres, S. V. Morozov, N. N. Mikhailov, S. A. Dvoretskii, and F. Teppe, Phys. Rev. Lett. **120**, 086401 (2018).

[23] M. S. Zholudev, F. Teppe, S. V. Morozov, M. Orlita, C. Consejo, S. Ruffenach, W. Knap, V. I. Gavrilenko, S. A. Dvoretskii, and N. N. Mikhailov, JETP Lett. **100**, 790 (2015).

[24] M. Orlita, B. A. Piot, G. Martinez, N. K. Sampath Kumar, C. Faugeras, M. Potemski, C. Michel, E. M. Hankiewicz, T. Brauner, Č. Drašar, S. Schreyeck, S. Grauer, K. Brunner, C. Gould, C. Brüne, and L. W. Molenkamp, Phys. Rev. Lett. **114**, 186401 (2015).

[25] V. Juričić, D. S. L. Abergel, and A. V. Balatsky, Phys. Rev. B **95**, 161403 (2017).

[26] G. Springholz and G. Bauer, in *Semiconductor Quantum Structures - Growth and Structuring*, Landolt-Börnstein Vol. III/34, edited by C. Klingshirn (Springer Verlag, Berlin, 2013), pp. 415–561.

[27] B. A. Assaf, T. Phuphachong, V. V. Volobuev, A. Inhofer, G. Bauer, G. Springholz, L. A. de Vaulchier, and Y. Guldner, Sci. Rep. **6**, 20323 (2016).

[28] See Supplemental Material at http://link.aps.org/supplemental/10.1103/PhysRevB.98.161202 for fan charts of $x = 0.14$ at 1.6 K, $x = 0.19$ at 1.6, 40, and 200 K, and the derivation of Eq. (5).

[29] D. L. Mitchell and R. F. Wallis, Phys. Rev. **151**, 581 (1966).

[30] R. L. Bernick and L. Kleinman, Solid State Commun. **8**, 569 (1970).

[31] G. Bauer, in *Narrow Gap Semiconductors Physics and Applications*, Lecture Notes in Physics Vol. 133, edited by W. Zawadzki (Springer, Berlin/Heidelberg, 1980), pp. 427–446.

[32] H. Burkhard, G. Bauer, and W. Zawadzki, Phys. Rev. B **19**, 5149 (1979).

[33] T. Phuphachong, B. A. Assaf, V. V. Volobuev, G. Bauer, G. Springholz, L.-A. de Vaulchier, and Y. Guldner, Crystals **7**, 29 (2017).

[34] A. J. Strauss, Phys. Rev. **157**, 608 (1967).

[35] G. Bauer, H. Pascher, and W. Zawadzki, Semicond. Sci. Technol. **7**, 703 (1992).

[36] H. Preier, Appl. Phys. **20**, 189 (1979).

[37] A. A. Abrikosov and S. D. Beneslavskii, J. Low Temp. Phys. **5**, 141 (1971).

[38] G. A. Baraff, Phys. Rev. **137**, A842 (1965).

[39] M. P. Vecchi, J. R. Pereira, and M. S. Dresselhaus, Phys. Rev. B **14**, 298 (1976).

[40] Z. Zhu, B. Fauqué, K. Behnia, and Y. Fuseya, J. Phys.: Condens. Matter **30**, 313001 (2018).